Simulation of the Rotorwash Induced by a Quadrotor Urban Air Taxi in Ground Effect

Denis-Gabriel Caprace*
Oak Ridge Associated Universities
NASA Ames Research Center
Moffett Field, CA, USA

Patricia Ventura Diaz
Science and Technology Corporation
NASA Ames Research Center
Moffett Field, CA, USA

Seokkwan Yoon
NASA Advanced Supercomputing Division
NASA Ames Research Center
Moffett Field, CA, USA

ABSTRACT

A rotorcraft hovering near the ground causes downwash and outwash. The impact of these induced velocities on urban air mobility operations has not been extensively quantified. This paper explores the opportunity of using CFD to perform dedicated studies on the aerodynamics of rotorcraft in ground effect (IGE). For this purpose, we compare load and flow predictions obtained with the high-fidelity CFD solver OVERFLOW and with a medium-fidelity vortex particle-mesh (VPM) method, for a single rotor IGE. We show that the computational cost of high-fidelity simulation makes it impractical to sweep through a large number of configurations or operating conditions. However, a small set of cases can be used to verify a medium-fidelity tool. The latter provides a better trade-off between "accuracy" and computational intensity, which enables numerous, longer simulations at a more affordable cost. As an example, the outwash flow is computed for two different designs of a quadrotor air taxi in hover and reveals the existence of increased velocities between the rotors. This work illustrates how CFD can help identify dangerous areas for passengers and ground personnel when they approach the vehicle.

NOTATION

c_n	$[-]$	:	sectional normal force coefficient
D	$[\mathrm{m}]$	:	rotor diameter
f_h	$[\mathrm{m\,s^{-1}}]$	:	outwash hazardousness factor
H	$[\mathrm{m}]$	:	rotor height above the ground
h	$[\mathrm{m}]$	:	grid spacing
R	$[\mathrm{m}]$	:	rotor radius
T_{rev}	$[\mathrm{s}]$	:	rotor revolution period
t_{end}	$[\mathrm{s}]$	:	physical time reached at the end of a simulation
U_{tip}	$[\mathrm{m\,s^{-1}}]$	:	blade tip velocity
$u_{x,y,z}$	$[\mathrm{m\,s^{-1}}]$	:	components of the velocity vector $\mathbf{u}$
V_H	$[\mathrm{m\,s^{-1}}]$	:	rotor induced velocity in hover
$\bar{V}_{\mathrm{max}}$	$[\mathrm{m\,s^{-1}}]$	:	maximum velocity in the wall jet
$z_{1/2}$	$[\mathrm{m}]$	:	thickness of the wall jet
Δt	$[\mathrm{s}]$	:	physical time step
ρ	$[\mathrm{kg\,s^{-3}}]$	:	air density
$\omega_{x,y,z}$	$[\mathrm{s^{-1}}]$	:	components of the vorticity vector $\boldsymbol{\omega}$

*NPP fellow. Corresponding author: denis-gabriel.caprace@nasa.gov
Presented at the Vertical Flight Society's 79th Annual Forum & Technology Display, West Palm Beach, FL, May 16–18, 2023.

INTRODUCTION

As with any VTOL aircraft, the aerodynamics of urban air mobility (UAM) vehicles operating close to the ground deserve special attention (Fig. 1). However, this is an area that has not yet been adequately studied for UAM. For conventional helicopters, rotorwash has been a recurring concern over the years. When located in ground proximity, a rotor blows air directly beneath the vehicle (downwash), and radial flow is also induced parallel to the ground (outwash). These induced velocities can be dangerous, especially when rotors have a high disk loading, because they can generate brownout —a phenomenon that lowers pilots' visibility by entraining particles (such as dust or snow) in the rotor wake. Another concern is the potential hazard created by the rotorwash itself, which may exert unacceptably high pressure directly onto ground personnel or cause loose objects (gravel, debris, etc.) to blow into them. For those reasons, rotorwash has been studied extensively in the context of military and civil helicopter operations close to the ground. Studies of such operations in the context of UAM are lacking.

Most studies so far have characterized downwash and outwash through the measurement of time-averaged velocity profiles at various locations with respect to the rotor disk. In most cases, statistics were collected for a rotor (or a system of

Figure 1: Illustration of a UAM vehicle in ground effect.

Figure 2: NASA Quadrotor Urban Air Taxi (Ref. 1).

rotors) in steady hover at various heights. Full-scale studies have been carried out, for example, in Refs. 2, 3, considering rotorcraft with various rotor arrangements (single rotor, tandem rotor, and tilt-rotor). Wind tunnel experiments have also been conducted. For example, Lee et al. (Ref. 4) studied how rotor tip vortices interact with the ground plane. Tanner et al. (Ref. 5) examined the outwash flow of a conventional helicopter configuration. Ramasamy and Yamauchi (Ref. 6) compared single and tandem rotors to highlight the effects of rotor arrangement on the measured velocity profiles. They also provided an extensive list of prior published experiments pertaining to ground effect. Dekker et al. (Ref. 7) studied the flow patterns in the vicinity of side-by-side rotors in ground effect.

Rotorwash is also being studied through CFD, the potential of which has not yet been fully explored (Ref. 8). Compared to out-of-ground effect (OGE) cases, high-fidelity body-resolved simulations tend to be even more computationally intensive because refined meshes (required to resolve the flow over an extensive ground region) and longer simulation times (necessary to wash out or dissipate the starting structures and obtain statistics) are required (Ref. 9). Therefore, examples of such simulations for downwash and outwash predictions are scarce. However, the stringent numerical requirement of CFD simulations can be relaxed if one accepts to model the presence of the rotor instead of capturing it in full, for example, using actuator disk (Ref. 10) or actuator line methods (Ref. 11). Similarly, medium-fidelity simulations have shown promising results (Refs. 12–14), and enable more extensive studies at a lower cost. Alternatively, hybrid simulation frameworks —aggregating a high-fidelity blade-resolved solver for the near-wake region and a vortex-based solver for the far wake— have also proven successful in reducing the computational cost while maintaining a sufficient level of accuracy (Ref. 15), compared to standalone high-fidelity simulations.

Despite the relatively wide body of literature on these topics for conventional helicopters, few studies have addressed the above concerns in the context of UAM. One challenging aspect of UAM vehicles is the variety of vehicle geometries, such as the tilt-wing configuration presented in Fig. 1 or the quadcopter in Fig. 2. This diversity necessitates the use of efficient computational tools to assess several different configurations in a finite time. This paper explores the opportunity of combining the use of medium and high-fidelity CFD to perform dedicated studies on the aerodynamic interaction of UAM vehicles in ground effect (IGE).

OUTLINE OF THIS RESEARCH

Since the computational cost associated with standalone high-fidelity simulation of hover IGE makes it impractical for use in an extensive rotorwash study, this work relies on two levels of fidelity. First, high-fidelity wall-resolved delayed detached eddy simulation (DDES) provides reference results. For this purpose, we use NASA's CFD code OVERFLOW, which is an established tool for accurate rotorcraft predictions. Recently, OVERFLOW simulations have brought new insights into the aerodynamics of UAM vehicles (Refs. 16–18). Furthermore, clear guidelines have now been established to guarantee the consistency and accuracy of CFD predictions with such high-fidelity codes, using either central difference (Ref. 19) or upwind (Ref. 20) schemes. Second, we employ a vortex particle-mesh (VPM) method: a medium-fidelity tool that enables longer simulations at an affordable cost. Although it has a longer history in the field of wind energy, multiple rotorcraft applications have recently been examined using the VPM method (Refs. 21–24).

This work focuses on a single rotor and a quadrotor IGE. The latter has received little attention in the literature compared to other configurations. First, the numerical predictions of each tool for the single rotor are compared. Results obtained with different numerical schemes and mesh resolutions are included in the comparisons. The underlying objective is to assess the computational cost versus accuracy ratio for different sets of numerical parameters. We aim to identify minimum requirements for outwash simulations that would enable sufficiently accurate computations (compared to a best-practice reference) while reducing their cost.

Subsequently, medium-fidelity simulations are used to verify the effect of the rotor height and thrust in the single rotor case. The quadrotor case is then addressed as a more relevant illustration for UAM applications. Simulations are performed for two different designs of the NASA quadcopter air taxi to investigate the effect of rotor placement (vertical offset) on the outwash. The hazard posed by the rotorwash is quantified in both cases by analyzing the average velocity and the amplitude of the fluctuations in a plane parallel to the

ground.

METHODS

High-fidelity Solver

The high-fidelity flow solver used in this study is OVERFLOW (Ref. 25). It is a finite-difference, structured overset grid flow solver. OVERFLOW solves the unsteady Reynolds-Averaged Navier-Stokes (RANS) equations for compressible flow in strong conservation form,

$$\frac{\partial \mathbf{q}}{\partial t} + \frac{\partial (\mathbf{F} - \mathbf{F}_v)}{\partial x} + \frac{\partial (\mathbf{G} - \mathbf{G}_v)}{\partial y} + \frac{\partial (\mathbf{H} - \mathbf{H}_v)}{\partial z} = \mathbf{0}, \qquad (1)$$

with $\mathbf{q} = [\rho, \rho u_x, \rho u_y, \rho u_z, e]^\intercal$ the vector of conserved variables, $\mathbf{F}$, $\mathbf{G}$, $\mathbf{H}$ the inviscid flux vectors in the three directions, and $\mathbf{F}_v$, $\mathbf{G}_v$, $\mathbf{H}_v$ the viscous flux vectors. In the present study, time marching implements the second-order backward difference formula with dual time-stepping, and an implicit formulation of the subiterations. The spatial discretization of the convective fluxes utilizes a fourth-order or a sixth-order accurate central difference scheme, while a third- or fifth-order artificial dissipation term is added for numerical stability. This added term uses either a scalar or a matrix form (Ref. 26). In the former, the same scalar-valued scaling factor is used for all six flow variables, based on the spectral radius of the flux Jacobian in the appropriate direction. In the latter, the scalar is replaced with the flux Jacobian matrix itself. Furthermore, the DDES capability of the code is employed, which combines the Spalart-Allmaras turbulence model close to the walls with a large eddy simulation (LES) formulation away from the wall. Details about turbulence modeling in OVERFLOW can be found in our previous works (Refs. 17, 27), and references therein.

NASA's Chimera Grid Tools (CGT) overset grid generation software is used to generate the overset grids of the rotors (Ref. 28). Body-fitted curvilinear near-body (NB) grids are generated using CGT. In practice, the same grids as in Ref. 17 are used for the present study (Fig. 3). The ground is considered as an infinite flat surface. An additional NB grid is used in the near-wall region directly underneath the rotor that extends laterally to a predefined radial distance. This wall grid is stretched in the wall-normal direction so that a no-slip boundary condition can effectively be enforced at the ground. The remainder of the computational domain is filled with Cartesian off-body (OB) grids that are automatically generated prior to grid assembly using the domain connectivity framework in OVERFLOW-D mode. For more details on the grid generation and assembly process, we refer again the reader to our previous publications (Refs. 17, 27).

Medium-fidelity Solver

The VPM method solves the Navier-Stokes equations for incompressible flow in their vorticity-velocity formulation,

$$\nabla \cdot \mathbf{u} = 0, \qquad (2)$$

$$\frac{D\boldsymbol{\omega}}{Dt} = (\nabla \mathbf{u}) \cdot \boldsymbol{\omega} + \nu \nabla^2 \boldsymbol{\omega} + \nabla \cdot \mathbf{T}^M, \qquad (3)$$

where $\mathbf{u}$ is the velocity, $\boldsymbol{\omega} = \nabla \times \mathbf{u}$ is the vorticity, $\frac{D}{Dt}$ denotes the Lagrangian derivative, ν is the kinematic viscosity, and $\mathbf{T}^M$ refers to the contribution of a sub-grid scale (SGS) model. The hybrid character of the VPM method comes from the combined use of a Lagrangian and a Eulerian discretization. On the one hand, vortex particles are employed to solve flow advection. The time integration here employs a third-order Runge-Kutta scheme. On the other hand, stretching and diffusion are solved on a background Cartesian grid through the use of fourth-order finite differences. The velocity field is computed by solving a Poisson equation,

$$\nabla^2 \mathbf{u} = -\nabla \times \boldsymbol{\omega}. \qquad (4)$$

The Poisson solver (Refs. 29, 30) takes advantage of the uniform grid resolution and operates in Fourier space, benefiting from an efficient 3D fast Fourier transform algorithm. As the particles move over time, high-order interpolation schemes are employed to exchange information between the particles and the grid. The SGS model used in this work is the regularized variational multiscale model (Ref. 31). It takes the same form as an eddy viscosity model but formulated for the vorticity,

$$\mathbf{T}^M = \nu_{\text{SGS}} \boldsymbol{Q}^{\boldsymbol{s}}, \qquad (5)$$

where $\boldsymbol{Q} = \nabla \boldsymbol{\omega}^s - (\nabla \boldsymbol{\omega}^s)^\intercal$. $\boldsymbol{\omega}^s$ is the resolved high-wavenumber content of the vorticity field. It is obtained using a recursive filtering operation which also takes advantage of the mesh. The model was calibrated by Cocle et al. (Ref. 32) and enables LES. The resulting method is known to have low dissipation and dispersion errors (Refs. 33, 34), while being computationally efficient on massively parallel architectures (Ref. 35). Another advantage of this hybrid framework is that the constraint on the time step is usually less stringent than the classical Courant-Friedrichs-Lewy (CFL) condition in Eulerian solvers (Ref. 36). The present implementation uses adaptive time-stepping to maintain a Lagrangian CFL (LCFL) number under a prescribed value, $\Delta t \leq \frac{\text{LCFL}}{||\nabla \mathbf{u}||_\infty}$. In the case of rotors, we also impose that $\text{CFL}_{\text{tip}} = \frac{U_{\text{tip}} \Delta t}{h} \leq 4$. More details on the VPM method and on its theoretical foundation can be found in the reviews of Refs. 34, 36, 37, and references therein. Additionally, a description of the present implementation on massively parallel architectures is provided in Ref. 35, based on the open-source PPM library (Ref. 38).

The aerodynamics rotors are modeled using Immersed Lifting Lines (ILL). The lift and drag of each section on the line are retrieved from the locally computed effective velocity $\mathbf{U}_e$, the corresponding angle of attack, and user-provided 2D airfoil tables. The local bound circulation $\boldsymbol{\Gamma}_b$ is then computed

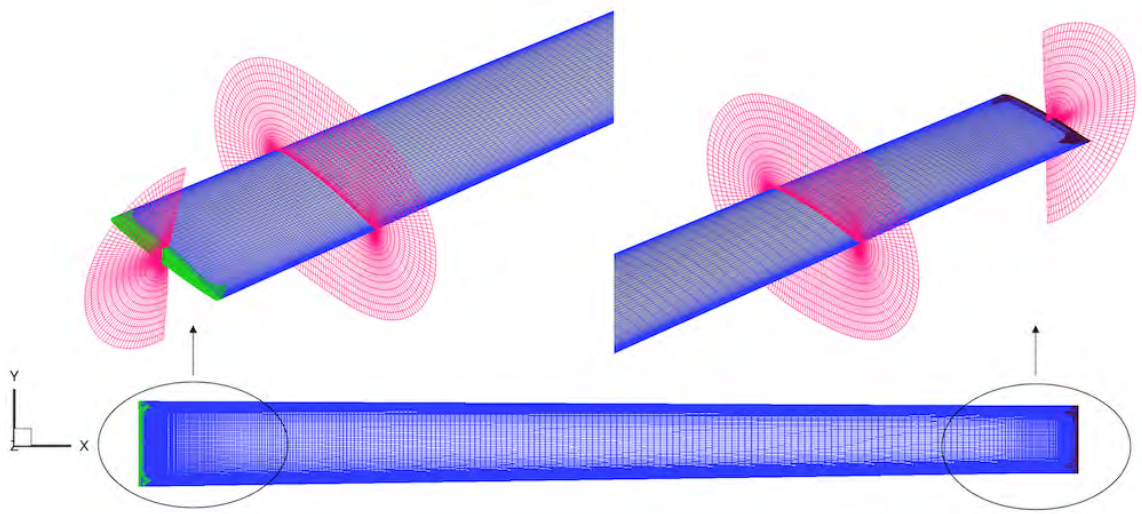

Figure 3: Overset grids of one blade of the quadcopter air taxi concept. Cap grids are used for the root (green) and tip (brown), and an O-grid is used for the blade (blue). Slices of the volume grids are shown in magenta. The surface mesh uses 200 grid points spanwise and 286 chordwise. Clustering is added near the leading edge, trailing edge, blade tip, and blade root, to resolve the large pressure gradients in these regions. The frame shown is local to the blade. Reproduced from Ref. 17.

from the Kutta-Joukowski equation,

$$\boldsymbol{\ell} = \rho \mathbf{U}_e \times \boldsymbol{\Gamma}_b, \tag{6}$$

where $\boldsymbol{\ell}$ is the sectional lift vector. The shed vorticity is then computed based on the spatial and temporal variations of the bound circulation, and introduced in the flow through the addition of particles. For brevity, we refer the reader to Ref. 39 for a detailed description of the ILL model.

A novelty of this work is the introduction of a no-slip boundary condition for the flat ground. Our implementation differs from the work by Zhao et al. (Ref. 12) who used a penalization technique, or Tan et al. (Ref. 13) who resorted to a discretization of the ground in panels. Instead, we use a procedure combining the method of images, which can be used to model an inviscid ground, and an additional treatment to effectively recover the no-slip condition. The procedure, which was first tested in Ref. 40, works as follows. For convenience, let us consider y as the wall-normal direction ($\hat{\mathbf{n}} = \hat{\boldsymbol{e}}_y$). We introduce the notation $q|_j = q(x, jh, z)$ where q is an arbitrary quantity on the grid, j denotes the grid index in the y direction (0 being at the wall), and we drop x, z for concision. At the beginning of the time step, the Poisson equation Eq. (4) is solved using symmetry conditions at the wall with even parity on the wall-normal vorticity and odd parity on the tangential vorticity. The resulting velocity field satisfies the no-through-flow condition $\mathbf{u} \cdot \hat{\mathbf{n}} = 0$, but a slip velocity may exist. A non-zero tangential vorticity component can however be computed at the wall in order to account for the no-slip condition. We first set the tangential components of the velocity to $u_x|_0 = U_x$, $u_z|_0 = U_z$, where U_x, U_z is the wall velocity (non-zero in case of a moving wall). Since the velocity is uniform at the wall, we have

$$\omega_x|_0 = \left.\frac{\partial u_z}{\partial y}\right|_0 \quad \text{and} \quad \omega_z|_0 = -\left.\frac{\partial u_x}{\partial y}\right|_0. \tag{7}$$

This allows us to connect the tangential vorticity at the wall with a Taylor expansion of the velocity. We use information from up to four points above the wall to maintain the fourth-order accuracy of the stencil,

$$\left.\frac{\partial u}{\partial y}\right|_0 = \frac{-25\,u|_0 + 48\,u|_1 - 36\,u|_2 + 16\,u|_3 - 3\,u|_4}{12h} - \mathcal{O}(h^4). \tag{8}$$

Finally, the ghost points of the vorticity field below the wall are adjusted to ensure no diffusion through the wall. The rest of the time step is performed as usual. Consequently, the tangential vorticity that we computed at the wall will diffuse into the flow, allowing a wall boundary layer to develop.

The VPM method has undergone a long history of verification and validation, including fundamental vortex dynamics (Ref. 41) and engineering applications such as wind turbine wakes (Ref. 42), and rotor loads in hover (Ref. 22) and edgewise flight (Ref. 24). Our new implementation of the ground plane is verified in the next section.

VALIDATION OF THE VPM NO-SLIP

The new boundary condition developed in this work is validated in the case of a turbulent channel flow at $Re_\tau = \frac{u_\tau \delta}{\nu} \approx 180$. The channel is defined with two walls located at $y = \pm d$. The mass flow is imposed in the x direction. The VPM simulation is set up in a domain of size $L_x \times L_y \times L_z = 3\delta \times 2\delta \times \delta$ with a uniform spatial resolution of 256 particles per δ.

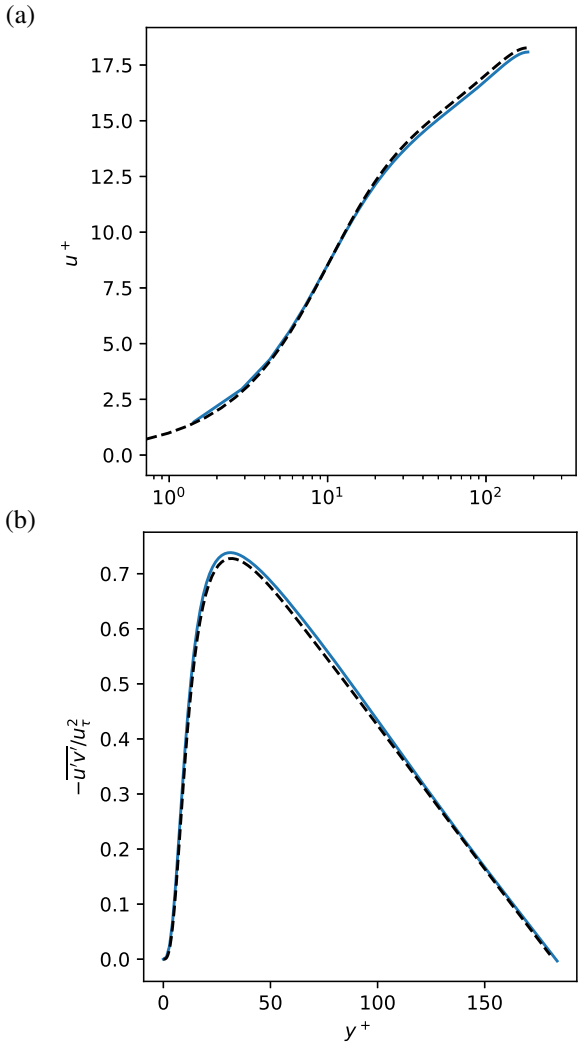

Figure 4: (a) Average velocity profile and (b) resolved turbulent stresses in the turbulent channel flow at $Re_\tau \approx 180$ obtained with VPM (—) compared to the DNS results of Ref. 43 (- -).

Statistics are collected after the transient necessary for the establishment of the flow, over a period of $10t_{\text{ref}}$, with $t_{\text{ref}} = \delta/u_\tau$.

We validate our results against the direct numerical simulation of Lee and Moser (Ref. 43). The wall friction computed from the simulation, $\frac{\tau_w}{\rho} = \nu\frac{d\bar{u}_x}{dy}$ leads to $u_\tau = \sqrt{\frac{\tau_w}{\rho}} = 0.06448$.

The velocity profile in wall variables ($u^+ = \frac{\bar{u}_x}{u_\tau}$) as a function of the distance from the wall ($y^+ = \frac{yu_\tau}{\nu}$) is shown in Fig. 4(a). The Reynolds stresses are also presented in Fig. 4(b). Excellent agreement with the reference simulation is observed. This demonstrates the proper implementation of the no-slip condition in the VPM framework and its ability to perform direct numerical simulation of wall-bounded flows.

COMPUTATIONAL SETUP

Rotor Geometry and Operating Conditions

We consider the rotor geometry of the NASA quadcopter urban air taxi concept (Fig. 2) described in Refs. 17, 27. A summary of the rotor properties is provided in Table 1, together with the parameters of the two operating conditions considered in this work. The rotor has three blades. Each blade is straight, linearly tapered, and built with modern thick airfoils. The blade twist is also linear, with $\theta = \Delta\theta(\frac{r}{R} - 0.75)$. The high-fidelity model of the rotor includes a rotor hub. It is not included in the medium-fidelity simulations.

All simulations are run with prescribed kinematics in both the medium- and high-fidelity frameworks. Two levels of thrust are considered. For each level, the pitch and flap angles are kept constant throughout the simulations, and the same values are used for the single rotor and the quadrotor configuration. The flap angle is arbirarily set to 0°. No airframe or fuselage is included in any of the simulations; we leave the study of rotor-airframe-ground interaction for subsequent work.

Table 1: Rotor geometry and operating conditions.

Geometry		
tip radius R	2.81	[m]
root cutout $\frac{R_i}{R}$	0.12	[–]
thrust-weighted solidity σ	0.0647	[–]
blade twist difference $\Delta\theta$	−12.0	[°]
blade taper ratio $c_{\text{tip}}/c_{\text{root}}$	0.81	[–]
Operating conditions		
rotation rate Ω	570.0	[RPM]
blade collective pitch angle θ_0		
thrust level 1	10.0	[°]
thrust level 2	12.5	[°]
blade collective flap angle β_0		
thrust level 1 & 2	0.0	[°]

High Fidelity Setup

Only the single rotor configuration is analyzed with the high-fidelity method in this work. A summary of the grid properties for the simulations of the single rotor IGE is presented in Table 2, and compared to the properties of an equivalent OGE grid. For both grids, the same surface meshes are employed for the rotor blades and hub, respectively. The wake resolution reported in the table corresponds to the nominal grid spacing in the wake-refinement region. For the IGE grid, this region extends from the ground to the height of the rotor and laterally to four radii away from the rotor in each direction. It also encompasses the direct vicinity of the rotor. For the OGE grid, the wake refinement extends to 1.4 radii below the rotor, 0.5 above, and 1.25 laterally. The table illustrates the substantial increase in the number of grid points necessary for the present outwash study.

Table 2: List of assembled grids for the high-fidelity simulations of the single rotor.

grid	height	wake res.	N grid points
IGE	R	$0.10c_{\text{tip}}$	439M
OGE	∞	$0.10c_{\text{tip}}$	77M

Figure 5 presents a cut in the IGE grid. It shows the OB grids and the wake-refinement region. The coarsening of the grid outside of the wake-refinement region can also be seen. The grid is coarsened until it reaches the characteristic outlet boundary conditions located 20 radii away from the rotor in all unbounded directions.

At the surface of the blades and hub, we verified that the maximum y^+ does not exceed one in all our simulations. Similarly, we always have $y^+ \leq 0.1$ at the ground plane.

The objective of the high-fidelity simulations is to collect statistics on the velocity in the wake-refined region. However, each simulation is initialized as an impulsively started flow. Since the initial transient is not of particular interest to this study, a procedure is employed to accelerate the simulation during the start-up until the establishment of the flow. The procedure is inspired by the guidelines published in Ref. 19 for the simulation of a hovering rotor OGE with OVERFLOW. The idea is to start the simulation by solving the flow in a quasi-time-accurate manner and with higher artificial dissipation. This way, the simulation progresses through the initial transient approximately 10 times faster than if it was computed in a fully time-accurate manner. The principle is the same for the simulations IGE since the starting vortex which forms initially must be evacuated before meaningful statistics can be collected. However, unlike OGE simulations, this vortex stays longer in the wake-refinement region because it interacts with vorticity in the boundary layer forming on the ground, and because the wake-refinement region itself is larger. Therefore, the simulations in this work were generally performed as follows. An initial simulation is run for 10 rotor revolutions with a time step corresponding to the rotation of the rotor by one degree, a fourth-order central difference scheme in the OB and NB regions, and a third-order artificial scalar dissipation term. This simulation is then restarted with the parameters initially intended for the simulation (discussed below), and serves to collect statistics. At each iteration, we use up to 50 dual-time sub-iterations to achieve a 2.5 to 3.0 orders of magnitude drop in the L_2 norm of the flow residuals.

The numerical approach and time stepping were previously validated for various rotor flows OGE (Refs. 44, 45). This work further aims to investigate the effect of the time step and the numerical scheme on the rotorwash results. Therefore, the overall order of the spatial discretization (i.e., the combined order of the convective and dissipation terms) will be varied separately in the NB and OB regions, respectively noted $\mathcal{O}_{\mathbf{NB}}$ and $\mathcal{O}_{\mathbf{OB}}$.

Table 3: List of grids for the medium-fidelity simulations of the single rotor.

grid	uniform res.	N particles
OGE	$R/32$	7M
IGE $L3$	$R/32$	19M
IGE $L2$	$R/48$	65M
IGE $L1$	$R/64$	153M

Medium-fidelity Setup

Because the background Cartesian grid has a uniform resolution, all VPM simulations utilize the same set of grids regardless of the rotor height. Grid sensitivity is assessed by comparing the results of VPM simulations at three different spatial resolutions, from 32 to 64 points per radius. The associated properties are shown in Table 3.

The domain size for the single rotor cases IGE is $6D \times 6D \times 2D$. The no-slip boundary condition is used at the wall. Notice that it is not intended to fully capture the boundary layer: this would require a much finer resolution. Instead, the coarsely-resolved no-slip condition is utilized as a model of the viscous ground, and the comparison with the high-fidelity CFD will allow us to verify the quality of this modeling approach. Unbounded boundary conditions are used for the lateral boundaries $(\pm x, \pm y)$ and the top boundary $(+z)$. More details on the boundary conditions in the VPM method and their implementation are discussed in Ref. 30.

The immersed lifting lines which model the rotor blades in the VPM simulation are fed with airfoil tables corresponding to the modern thick profile used on the blades. These airfoil tables, formatted as standard `c81` files, describe the lift and drag coefficient as a function of Reynolds number and angle of attack, obtained experimentally.

RESULTS

Single Rotor

This section considers the single rotor and discusses the sensitivity of the rotor loads and downwash/outwash results to various parameters in OVERFLOW and VPM simulations.

Table 4 lists the OVERFLOW simulations that are analyzed and reports the main computational parameters along with the physical time reached at the end of the simulation t_{end}. All the simulations utilize the same IGE grid reported in Table 2. For high-fidelity DES simulations, previous works have demonstrated that the accurate computation of the figure of merit (FoM) requires high-order schemes in the NB grids, a grid spacing of at most 10% of the tip chord in the wake-refinement region, and a time step no longer than the time needed for the rotor to rotate by 0.25° (Ref. 19). The three simulations satisfy the criteria on the order of the schemes (≥ 4 in the NB grids) and on the grid resolution.

The high-order matrix dissipation (OF-HOMD) case is considered the baseline. It uses a time step compatible with the above guidelines, a fourth-order discretization in both the

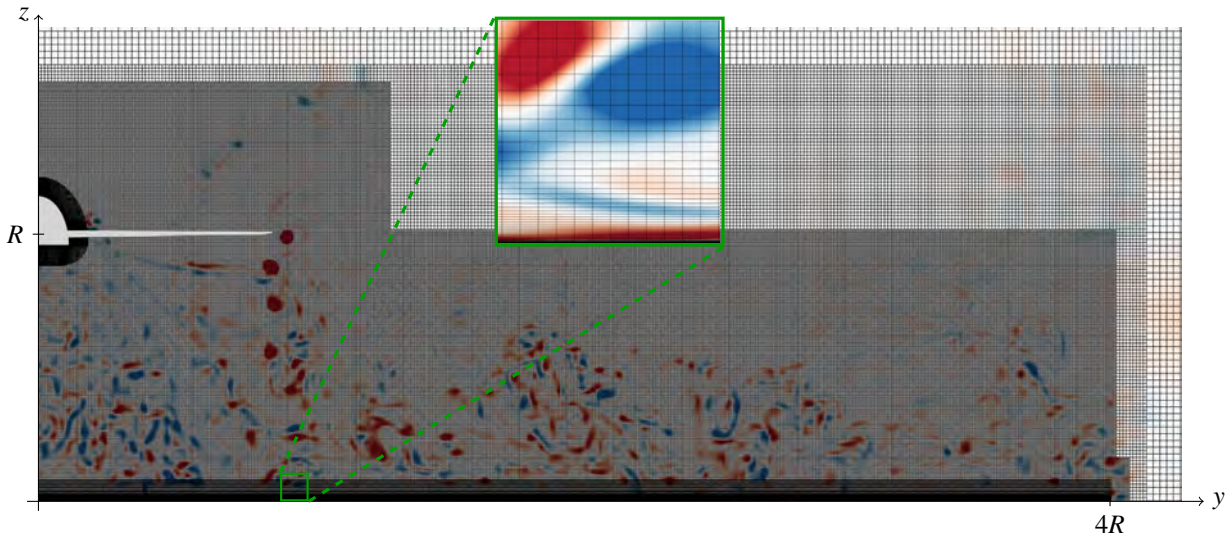

Figure 5: Cut through the OVERFLOW mesh superimposed with an instantaneous snapshot of the vorticity ω_x.

Table 4: List of OVERFLOW single rotor simulations.

label	$\mathcal{O}_{\mathrm{NB}}$	$\mathcal{O}_{\mathrm{OB}}$	dissip.	$\frac{t_{\mathrm{end}}}{T_{\mathrm{rev}}}$	$\frac{360\Delta t}{T_{\mathrm{rev}}}$
OF-HOMD	4	4	matrix	40	0.25°
OF-HOSD	5	5	scalar	50	1.00°
OF-LOSD	5	3	scalar	50	1.00°

Table 5: List of VPM single rotor simulations.

label	grid	H	θ	$\frac{t_{\mathrm{end}}}{T_{\mathrm{rev}}}$	$\frac{360\Delta t}{T_{\mathrm{rev}}}$ *
VPM-L3	IGE $L3$	R	10.0°	100	7.2°
VPM-L2	IGE $L2$	R	10.0°	100	5.4°
VPM-L1	IGE $L1$	R	10.0°	100	3.6°
VPM-H_2	IGE $L2$	$2R$	10.0°	100	5.4°
VPM-θ_2	IGE $L2$	R	12.5°	100	5.4°
VPM-OGE	OGE	∞	10.0°	30	5.4°

* average value, actual time step is adaptive.

NB and OB grids, and matrix dissipation. We consider this case as the most accurate available prediction, and we use it as a reference throughout the rest of this study, when compared with other OVERFLOW or VPM runs.

With the other two OVERFLOW cases, high-order scalar dissipation (OF-HOSD) and low-order scalar dissipation (OF-LOSD), we explore the possibility of reducing the computational cost of the outwash simulation by relaxing some of the criteria. As shown in the table, both OF-HOSD and OF-LOSD use a larger time step, while the latter also employs a third-order discretization in the OB grids. The accuracy of the predicted FoM will of course be deteriorated, but we aim to quantify the effect of the time step and the numerical scheme on the outwash predictions.

VPM simulations are also run with various parameters reported in Table 5. The main goal is to quantify the accuracy of the VPM predictions compared to the OVERFLOW baseline (OF-HOMD) by studying their sensitivity to the background grid resolution. The effect of the rotor height and disk loading is also considered.

Note that, since the VPM method is less computationally intensive than OVERFLOW, it was possible to compute 100 rotor revolutions in a reasonable time. The duration of the OVERFLOW simulations was limited by practical constraints in the schedule of the present writing. We comment more on the computational cost of the simulations at the end of this section.

A 3D view of the flow around the single rotor IGE obtained with OVERFLOW and the VPM method is shown in Fig. 6. The interaction between the rotor wake and the ground results in the wall region being filled with many vortical structures of various sizes. Their effect on the rotor loads and outwash are discussed next.

Loads The rotor load distribution is computed as the time-averaged, rotor-normal loading on the blade, shown in Fig. 7. The time averaging of the loads is done over a period corresponding to five rotor revolutions in all cases. The VPM results at all resolutions agree well with the reference OVERFLOW simulation, except in the tip region. Previous experience with the ILL model implemented in the VPM solver (Ref. 22) has shown that this behavior is caused by the difficulty for the ILL to accurately predict the blade-vortex interaction (BVI). The effect of the preceding tip vortex on the blade is not fully captured because of the model misses the details associated with the local three-dimensionality of the flow at the chord-size scale. It is worth noting that the model correctly predicts the trends in the loading, with a peak in the loading towards the tip. However, the amplitude of the peak is generally overpredicted, and has a non-monotonous dependency on the spatial resolution. The effect of the tip loads discrepancy on the time-average flow is discussed in the next paragraphs.

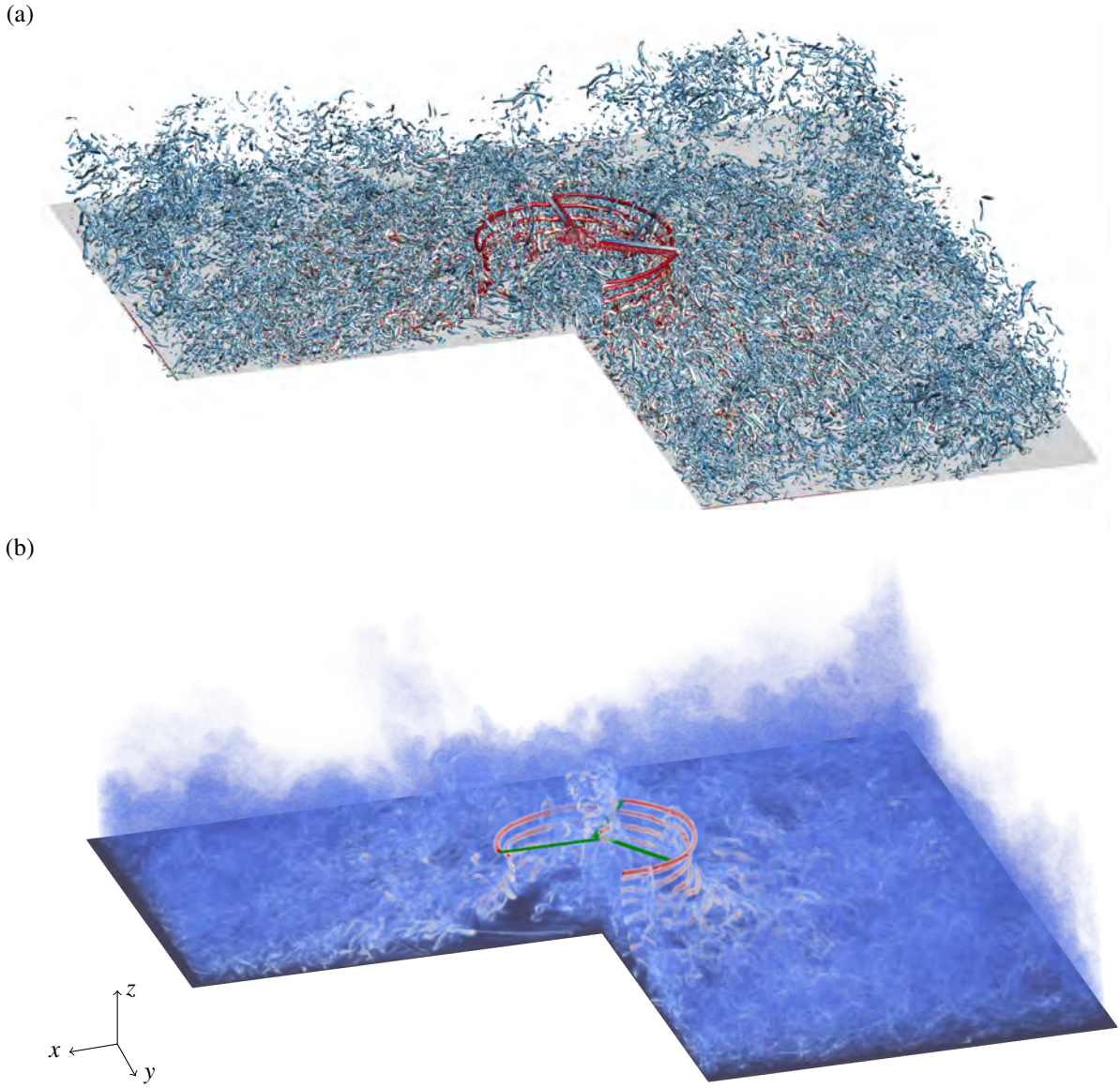

Figure 6: 3D view of an instantaneous snapshot of the simulations: (a) isocontour of the Q-criterion colored by the vorticity magnitude in OVERFLOW (OF-HOMD); (b) volume rendering of the vorticity magnitude in VPM (VPM-L1).

Time-averaged flow A time-averaged flow field obtained from each solver is shown in Fig. 8. As described in previous research (Refs. 2, 6), the flow can be subdivided into different regions. The region directly beneath the rotor is dominated by the downwash of the rotor and is characterized by a contraction of the vein emanating from the rotor. Closer to the wall, the downwash transitions to outwash as the flow entrained by the rotor is deviated radially by the wall. Subsequently, a jet forms along the wall in the outwash region.

Because of the breakdown of the tip vortices and the turbulent jet that develops in the outwash region, long averaging periods are required for the statistics collected in the wake to converge. From visual inspection of the vorticity field (similar to those shown in Fig. 6), we determined that the starting structure is well evacuated from the region of interest ($r < 4R$) after $t/T_{\text{rev}} = 50$. Considering the physical time reached at the end of the simulations (shown in the last column of Tables 4 and 5), all the flow averages from the VPM simulation were computed over a period corresponding to the last 25 rotor revolutions. However, since OVERFLOW simulations reached a smaller t_{end}, there is a trade-off between getting well-converged statistics and mitigating the effect of the starting structure on the statistics. Therefore, the averaging is performed over the last 10 rotor revolutions in the OVERFLOW simulations. To increase the size of the ensemble, the axisymmetry of the flow is exploited by incorporating data from both sides of the rotor in x- and y-slices. The influence of the averaging period on the outwash results is further discussed at the end of this section.

Downwash The streamline from the tip of the rotor blade materializes the limit between the flow entrained by the rotor

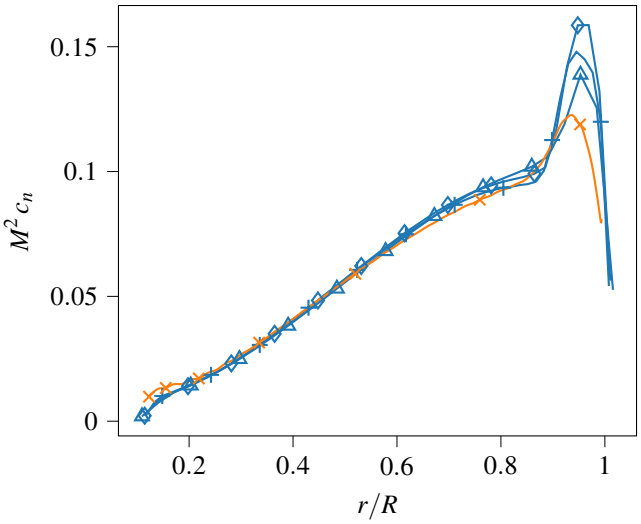

Figure 7: Blade normal loads on the single rotor at $H/R = 1$ for OF-HOMD ( ), VPM-L3 ( ), VPM-L2 ( ) and VPM-L1 ( ). For readability, markers are not drawn at every data point.

and the surrounding quiescent flow. We use it as a proxy for the average trajectory of the tip vortices. Figure 9 compares the streamtrace computed based on the average velocity in all cases. The OVERFLOW results only show a very small sensitivity to the numerical scheme and time step. The streamtraces are consistent over their entire length. On the other hand, the sensitivity of the VPM results to the mesh resolution is more pronounced. The mesh refinement brings the solution closer to the reference OVERFLOW case in the downwash region, but farther away in the outwash region. It should be noted that this diagnostic accumulates the error on the average velocity and the error committed by the streamtrace integration itself. The latter depends on the mesh resolution as well.

The contraction of the vein is maximum between $0.2R$ and $0.3R$ below the rotor (or, equivalently, a height of $0.8R$ and $0.7R$ above the ground), which is consistent with the experimental results reported in Ref. 9. At that location, the downwash velocity must be the highest. We compare the downwash based on the average vertical velocity profile at a distance of $0.25R$ below the rotor. It is plotted against the radial distance in Fig. 10. All simulations predict some upwash for radial distances smaller than $0.25R$. That region is also affected by the rotor hub (present in the OVERFLOW simulations, absent in VPM's) which may explain the difference in the trends towards the root. The agreement between all the cases is otherwise good over a large portion of the blade, with a somewhat smaller downwash predicted in the VPM results. However, towards the tip, larger discrepancies are observed between the various VPM cases, whereas the agreement between the OVERFLOW cases remains good. This behavior is directly related to the discrepancy in the load predictions. For example, the VPM-L3 case has a smaller peak in the tip load and a coarser resolution, indicative of larger and weaker tip vortices. The VPM-L1 case has a taller peak and a finer resolution, which is associated with stronger and smaller tip vortices. Correspondingly, the velocity gradient between the rotor downwash region and the outside of the vein is sharper.

Except for the details at the tip, the downwash predictions remain consistent with a maximum downward velocity about twice as large as the reference induced velocity in hover V_H.

Outwash The jet forming in the outwash region can be characterized using two parameters: a characteristic velocity $\bar{V}_{\max}$ and a characteristic thickness $z_{1/2}$. At a given radial location, $\bar{V}_{\max}$ is the maximum velocity across the height in the average outwash velocity profile. $z_{1/2}$ is the location where the velocity profile reaches half of $\bar{V}_{\max}$ in the upper region of the jet. As shown by Glauert (Ref. 46) and verified experimentally in several works including Ref. 6, the established jet velocity profile is self-similar when normalized with these quantities.

Figure 11 shows that the maximum velocity in the jet occurs at $r/D = 0.8$ and is consistently predicted by all the simulations. The magnitude of the peak, however, differs. The OF-LOSD and OF-HOSD cases predict a slightly higher peak compared to the reference OF-HOMD simulation. The VPM simulations predict lower maximum velocities compared to OVERFLOW, even more so when the spatial resolution increases.

The jet minimum thickness is reached around $r/D = 1.0$. The computed $z_{1/2}$ is very consistent between all the simulations up to that location. The VPM-L3 then underpredicts the growth rate of the jet, while the other predictions remain consistent. After $r/D = 1.75$, the OF-HOMD case shows a rapid increase in $z_{1/2}$. This is an artifact due to the starting structure which is still in the wake-resolved region between 30 and 40 revolutions of age (the period used for averaging). It is not seen in the other cases for which the statistics were collected at a later physical time in the simulation. Note that the "stairs" observed on all the $z_{1/2}$ curves reflect the grid resolution of each case, as our processing of the velocity profile identifies the discrete location on the grid where $\bar{u}_x$ becomes larger than $\frac{1}{2}\bar{V}_{\max}$ (i.e., the definition of $z_{1/2}$).

The predicted locations for the maximum velocity and minimum thickness agree qualitatively well with the experimental results in Ref. 9. The magnitude of $\bar{V}_{\max}$ also spans the same range as the experimental values. However, $z_{1/2}$ is approximately 1.5 times smaller than in the experiment. This is most likely due to the difference in rotor height between our computational setup and the experiment.

Velocity profiles are shown at the bottom of Fig. 11, normalized by the jet characteritic values. The agreement between all simulations is generally good, but it deteriorates for $z/z_{1/2} > 1$ when the radial distance increases. In particular, the VPM results are in good agreement with the OVERFLOW predictions. This is quite remarkable considering that none of the VPM simulations is fine enough to properly capture the wall boundary layer. This demonstrates that underresolved VPM simulations can indeed be used as a model to predict the interaction between the rotorwash and the ground.

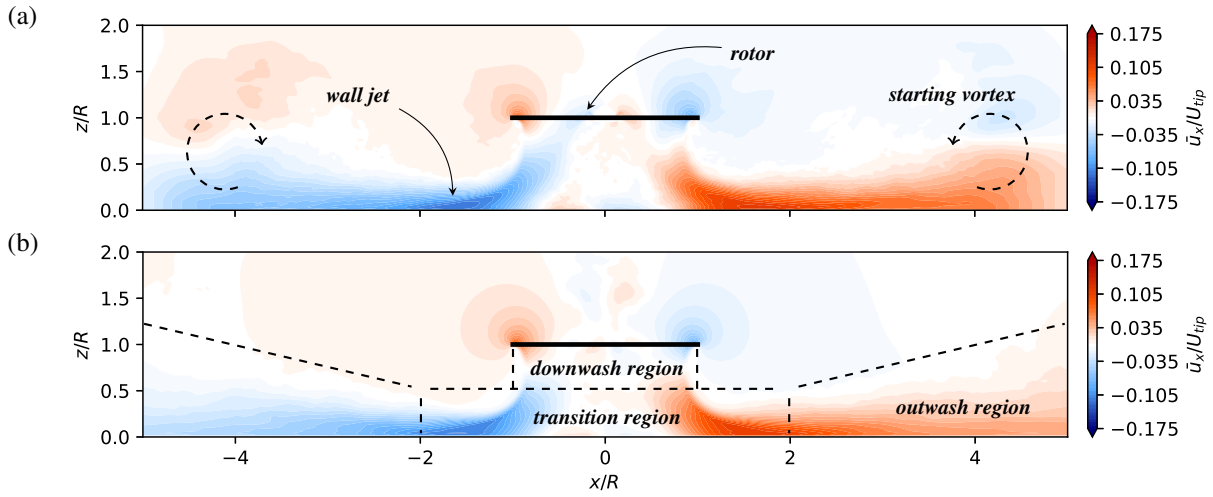

Figure 8: Time-averaged outwash velocity ($\bar{u}_x$) induced by the rotor hovering at one radius above the ground: (a) OF-HOMD, averaged over the last 10 revolutions; (b) VPM-L2, averaged over the last 25 revolutions.

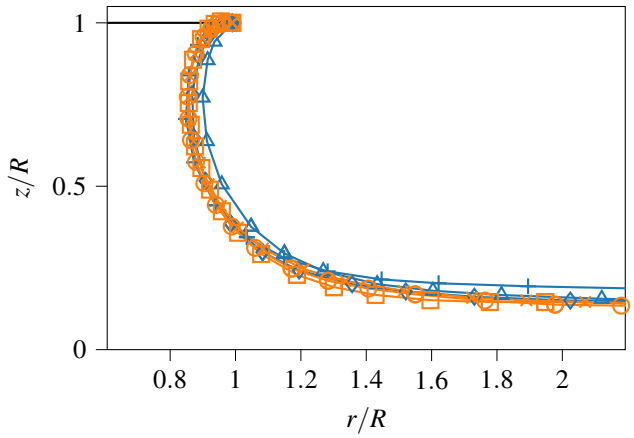

Figure 9: Streamtrace of the time-averaged flow starting at the blade tip: OF-LOSD ( ), OF-HOSD ( ), OF-HOMD ( ), VPM-L3 ( ), VPM-L2 ( ) and VPM-L1 ( ).

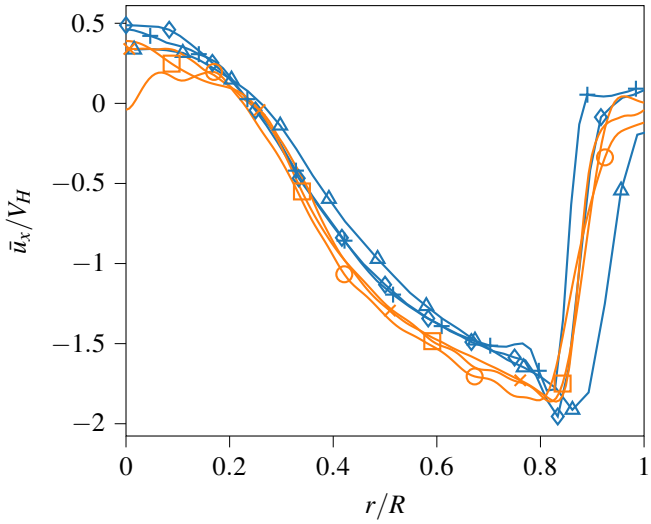

Figure 10: Downwash velocity profile based on the time-averaged flow at a distance of $0.25R$ below the rotor.: OF-LOSD ( ), OF-HOSD ( ), OF-HOMD ( ), VPM-L3 ( ), VPM-L2 ( ) and VPM-L1 ( ).

For $r/D \geq 1.0$ (i.e., when the jet is established), the velocity profiles become self-similar, as can be seen from the last two plots at the bottom right of Fig. 11. It should be noted that the established velocity profile, when normalized with $\bar{V}_{\max}$ and $z_{1/2}$, is relatively insensitive to the rotor loading and twist distribution (Ref. 9), which makes it possible to compare profiles across different rotors of various scales. Data from two experimental campaigns on the rotor of a CH-47D are overlayed in the figure: measurements collected at full-scale in Ref. 47, and the envelope of the measurements reported at model-scale in Ref. 9. The profiles from our computations agree well with these experimental data.

In addition to the diagnostics based on the average velocity field we analyzed so far, we examine the fluctuations of the velocity in the transition and outwash regions. Figure 12 presents the standard deviation of the velocity $u_{\text{std}} = \sqrt{\frac{2}{3}k}$ where the kinetic energy of the fluctuations $k = \frac{1}{2}\left(\overline{u_x'^2} + \overline{u_y'^2} + \overline{u_z'^2}\right)$, and $\mathbf{u}' = \mathbf{u} - \bar{\mathbf{u}}$. High fluctuations are often reported in the rotorwash (Ref. 47), which is confirmed by a u_{std} that amounts to 25% of $\bar{V}_{\max}$ in the established jet. In the transition region at $r/D = 0.4$, u_{std} has a marked peak at around $z/z_{1/2} = 1.8$. This peak is aligned with the location where the average velocity is the most negative, indicating that vortical structures are entrained in a recirculation. At $r/D = 0.6$, another peak is visible, this time associated with the passage of the tip vortices.

Compared to the average velocity, u_{std} features a larger variability across all the simulations. As far as OVERFLOW is concerned, the OF-LOSD case tends to slightly underpredict u_{std} compared to the reference OF-HOMD case; while the OF-HOSD case overpredicts it. Note that, since u_{std} is a sta-

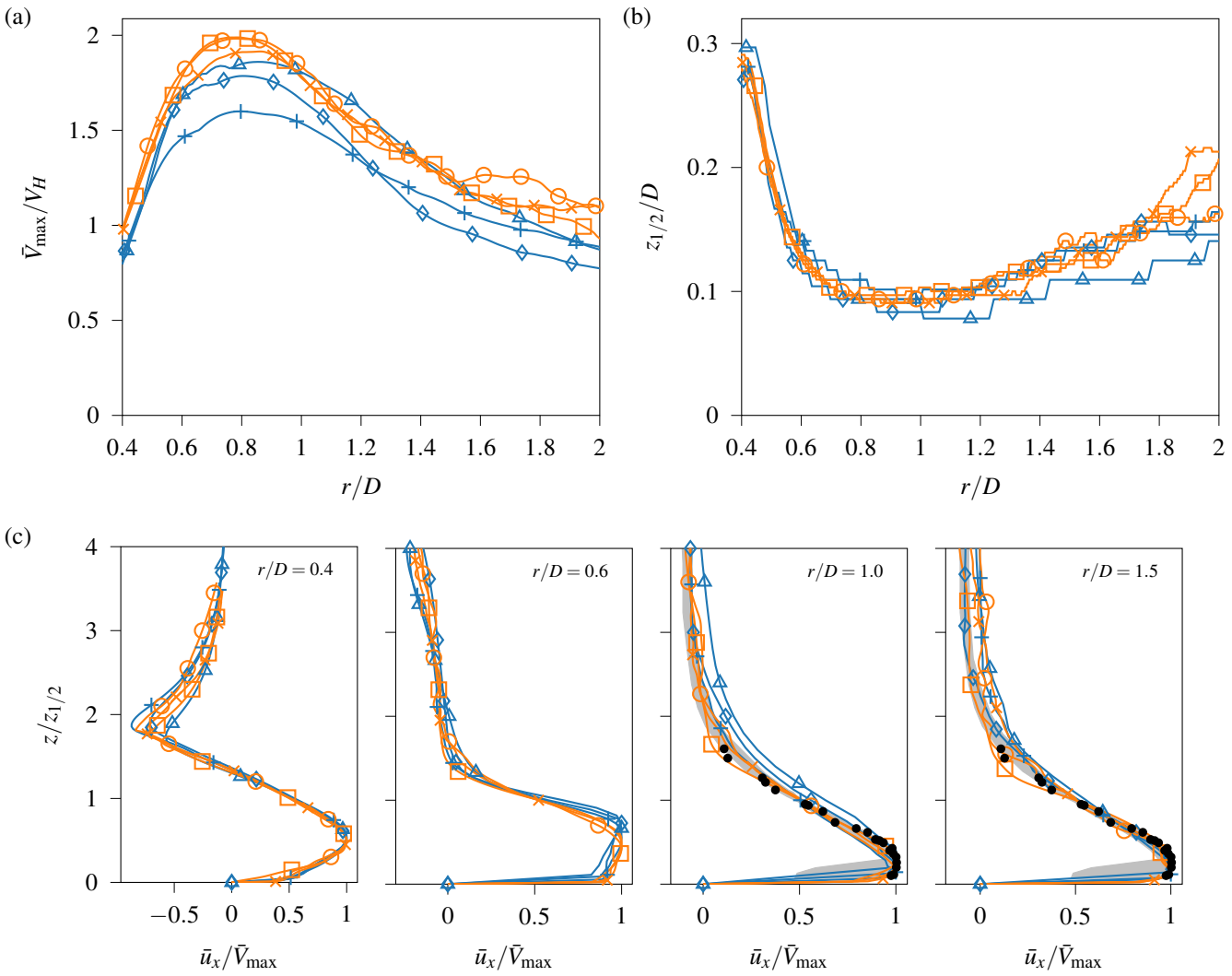

Figure 11: (a) Maximum outwash velocity, (b) thickness of the wall jet, and (c) outwash velocity profile at increasing radial locations (bottom): OF-LOSD ( ), OF-HOSD ( ), OF-HOMD ( ), VPM-L3 ( ), VPM-L2 ( ) and VPM-L1 ( ). Experimental data from Ref. 47 ( ) and Ref. 9 ( ) are also shown in the self-similar portion of outwash profile.

tistical moment of higher order compared to the velocity average, it converges slower. These curves would therefore benefit from longer averaging periods that would likely remove some of the oscillations they exhibit. Statistical convergence is further discussed at the end of this section.

Regarding the VPM simulations, it is again remarkable that the shape of the u_{std} profiles from the VPM simulations agree well with these from the OVERFLOW simulations, despite not accurately capturing the wall boundary layer. The best agreement is observed between VPM-L1 and OF-HOMD. On the other hand, the coarser resolution cases tend to underpredict u_{std} in the transition region and overpredict it in the jet.

As a conclusion regarding the sensitivity of the outwash results to the numerical parameters, only small differences were observed across the three OVERFLOW simulations. The largest discrepancies were seen on the computed $\bar{V}_{\max}$ and u_{std}. As far as the average velocity is concerned, these differences are likely small enough to justify the use of lower order schemes in the wake region and larger time steps if one is solely interested in predicting the outwash, provided it makes the simulation more computationally affordable. The cost of the simulations is discussed hereafter.

Regarding the VPM simulations, their predictions are generally in good agreement with the OVERFLOW reference case (OF-HOMD). The largest discrepancies were observed on $\bar{V}_{\max}$ at the higher resolution, and is possibly related to the discrepancy in the tip load prediction. For the same reason, the intermediate resolution provided the best agreement. Consistent velocity fluctuations were also observed compared to OVERFLOW, and the quality of the prediction improved with spatial resolution.

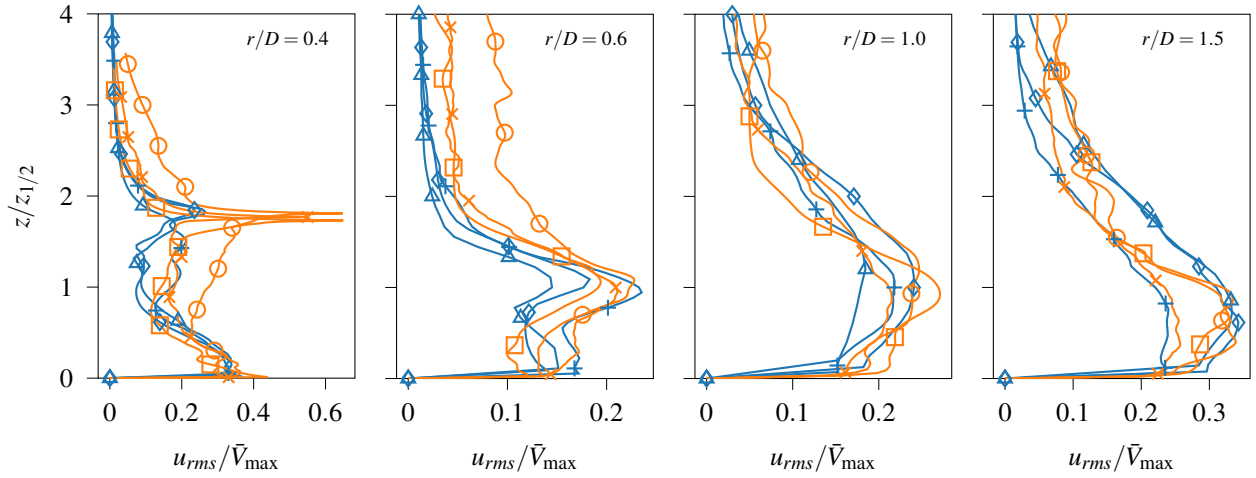

Figure 12: Velocity fluctuations in the wall jet at increasing radial locations: OF-LOSD ( ), OF-HOSD ( ), OF-HOMD ( ), VPM-L3 ( ), VPM-L2 ( ) and VPM-L1 ( ).

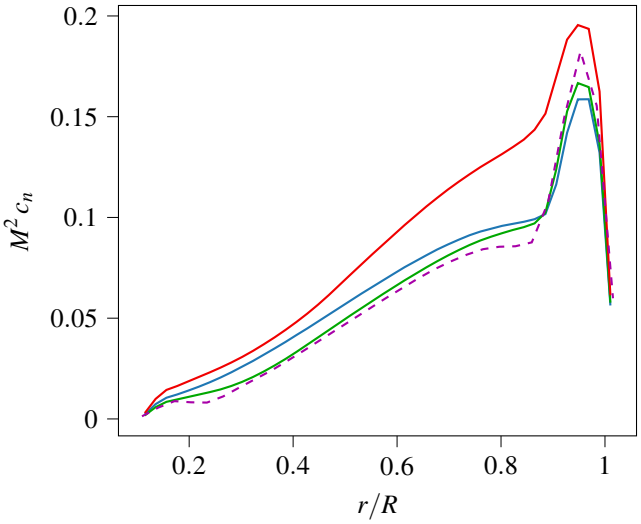

Figure 13: Blade normal loads for VPM-L2 (—), VPM-H_2 (—), VPM-θ_2 (—) and VPM-OGE (- -).

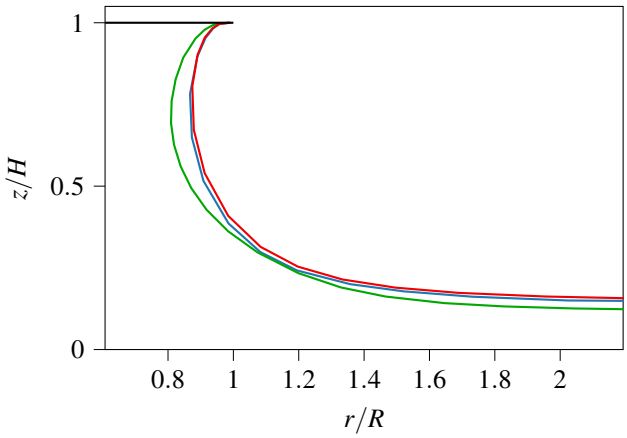

Figure 14: Streamtrace of the time-averaged flow starting at the blade tip: VPM-L2 (—), VPM-H_2 (—), and VPM-θ_2 (—).

Effect of height and disk loading Two additional ground-effect cases are simulated with the VPM method to illustrate the effect of height and disk loading on the results. The *L2* resolution is chosen for these cases and all subsequent simulations in this paper, since it provides the best trade-off between accuracy and computation cost. The reader is referred to Table 5 for a summary of the cases.

The blade normal loading is shown in Fig. 13. As expected, decreasing the height of the rotor above the ground increases the normal loading for a given pitch setting. The reference loading for the same rotor OGE is also shown. While the loading increases over most of the span with the reduced height, it is worth noticing that the amplitude of the peak load at the tip decreases. This indicates a modification in the trajectory of the tip vortices when the rotor comes close to the ground. Figure 14 confirms that the flow vein contracts less when the rotor height decreases, which must be associated with the tip vortices traveling more outboard of the rotor and passing further away from the next blade, reducing the effect of the BVI. On the other hand, the case with a higher blade pitch angle features an increased normal load over the whole blade radius, but has a relatively smaller amplitude peak. The corresponding limiting streamline remains close to that of the case at the same height and lower thrust (VPM-L2). Although we expect the VPM results to correctly capture the vortex trajectories and the trends in the loading, the actual amplitude of the peak load at the tip is subject to an error in the BVI prediction, as explained before. Incidentally, we note that, for all cases, the maximum contraction of the vein is still observed at a similar fraction of the rotor height, again between 70 and 80%. Compared to the OGE case, the overall thrust is increased by 2.3% (VPM-H_2), 8.7% (VPM-L2), and 40.9% (VPM-θ_2), respectively. The numbers obtained for VPM-H_2 and VPM-L2 agree qualitatively well with textbook predictions of ground effect.

Figure 15 presents the wall jet properties for the two new cases, VPM-H_2 and VPM-θ_2, compared to the reference VPM-L2. The increased rotor height yields a smaller

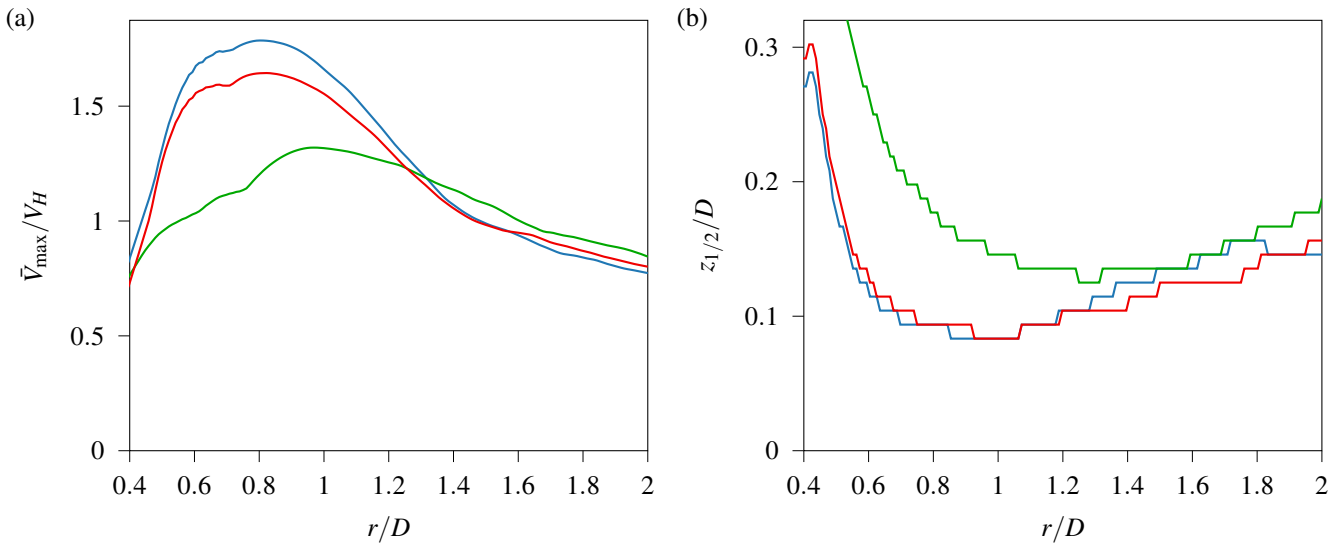

Figure 15: (a) Maximum outwash velocity and (b) thickness of the wall jet for VPM-L2 (—), VPM-H_2 (—) and VPM-θ_2 (—).

top maximum velocity and a larger jet thickness everywhere. Both quantities reach their extremum value at larger radii: $r/D \approx 1.0$ for $\bar{V}_{\max}$ (vs. 0.8 for the reference) and $r/D \approx 1.2$ for $z_{1/2}$ (vs. 1.0). However, we note that the maximum velocity observed at $r/D > 1.25$ in the VPM-H_2 case becomes larger than in the reference case. This is consistent with the behavior observed experimentally by Ramasamy and Yamauchi (Ref. 6).

The case with increased rotor thrust (VPM-θ_2) features a $\bar{V}_{\max}/V_H$ ratio generally smaller than the reference, but the additional thrust induces a larger V_H. $z_{1/2}$ is larger for $r/D < 1$ and smaller when the jet is established, although the differences with respect to VPM-L2 are small.

Note on Statistical Convergence

To add to the comments made so far about the statistical convergence, we illustrate the sensitivity of the time-averaged results to the number of rotor revolutions used in the averaging. Figure 16 shows the velocity profiles at the beginning of the outwash region for averaging periods from two to 50 rotor revolutions.

The convergence of the statistics is visible, as the profiles become smoother when the number of revolutions used for averaging increases. From the perspective of the VPM results, at least 10 rotor revolutions are necessary to capture the peak of the averaged velocity profile within 2.5% of the value obtained with averaging over 50 revolutions. As mentioned above, the convergence of u_{std} is slower. Discrepancies are still noticeable between the 10 and 50 revolutions averaging. Similar conclusions can be drawn from the OVERFLOW results, although the 50 revolutions averaging is not available for comparison due to the limited duration of the corresponding simulation.

We conclude that a minimum of 10 rotor revolutions should be used for the averaging of outwash results from CFD simulations. Ideally, an even larger number of revolutions should be used, especially when higher statistical moments are investigated, such as the standard deviation of the velocity. Moreover, let us recall that the averaging was here performed using velocity data collected in two perpendicular planes (normal to x and y) and using the left-right symmetry in each plane to increase the size of the ensembles.

Note on the Computational Cost

A comparison of the computation times for the single rotor simulation IGE is shown in Table 6. For the OVERFLOW simulations, an estimate of the computation time necessary to reach 100 rotor revolutions is provided, obtained by scaling the actual computation time. This allows us to compare the six cases. All the OVERFLOW simulations were run on 2000 Intel IvyBridge processors (Xeon E5-2680v2, CPU clock at 2.8GHz). The VPM simulations were run on 144 (VPM-L3) or 288 (VPM-L2 and VPM-L1) Intel Haswell processors (Xeon E5-2680v3, CPU clock at 2.5GHz).

Table 6: Compared computation time. CT_{end} is the computation time spent to reach the physical time t_{end}. $CT_{100\text{rev}}$ is the estimated computation time it would take to reach a physical time corresponding to 100 rotor revolutions.

label	$\frac{t_{\text{end}}}{T_{\text{rev}}}$	CT_{end} $[cpuh]$	$CT_{100\text{rev}}$ $[cpuh]$
OF-LOSD	50	0.85M	1.70M
OF-HOSD	50	0.90M	1.79M
OF-HOMD	35	1.62M	4.63M
VPM-L3	100	0.87k	–
VPM-L2	100	4.36k	–
VPM-L1	100	14.1k	–

Regarding the OVERFLOW cases, going from third to

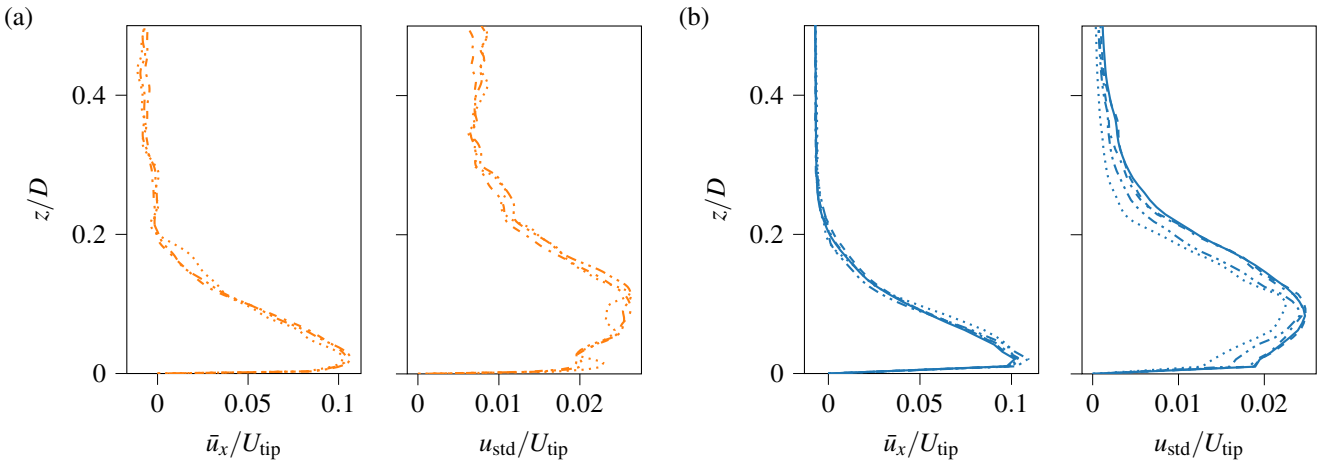

Figure 16: Influence of the averaging period on $\bar{u}_x$ and u_{std} at $r/D = 1.0$: (a) OF-HOSD case in orange and (b) VPM-L1 case in blue. The averaging is done over the last 2 (·····), 5 (··–), 10 (·–·), 25 (– –) and 50 (—) revolutions.

fifth order in the OB grids increased the computation time by approximately 5%. Since both simulations used 50 subiterations to converge the residuals at each time step, the difference is mainly due to the added cost of the higher-order scheme. The introduction of matrix dissipation increased the simulation cost by another 150%. This is due to the combined effect of a reduction in the physical time step, a smaller number of subiterations per time step, and the added cost of the matrix dissipation scheme.

It is worth mentioning that the start-up procedure of the OVERFLOW simulations (discussed in the computational setup section) could be improved to further reduce the time-to-solution. In particular, our results showed that the initial transient of the simulation and the associated starting vortex can affect the outwash results two diameters away from the rotor until the age of 35 revolutions. It is thus desirable to run the start-up simulation for an equivalent of at least 35 revolutions and evacuate the starting structures prior to running the time-accurate simulation with the intended high-fidelity parameters. Note that the duration of the initial transient also depends on the height of the rotor and the loading of the blade. The efficacy of this strategy will be assessed in future work.

When comparing the time to run the VPM simulation versus OVERFLOW, even the finest VPM case is 330 times faster than the baseline OF-HOMD case. Considering the good agreement we observed between the VPM and the reference DDES results, this demonstrates the viability of using the VPM method for ground effect and rotorwash computations. However, in addition to the code-to-code comparison that we presented in this work, we identify the need for further dedicated validation based on experimental results before the method can be confidently applied to a larger variety of cases.

Quadrotor

Following the code-to-code comparison of results on the single rotor presented above, the VPM method is used to compute the outwash flow in the case of a quadrotor air taxi. Two quadrotor designs are simulated to illustrate how medium-fidelity CFD can help us gain insight into the effect of vehicle design parameters on outwash considerations. For this example, we consider two design iterations of NASA's quadrotor air taxi concept (Fig. 2) with different rotor arrangements. In the first iteration, all the rotors are in the same plane. In the second, the rear rotors are mounted higher in order to reduce the effect of the wake-rotor interaction in forward flight (Ref. 17). This vertical offset is the only design parameter that we consider in this preliminary investigation.

For simplicity, the rotors in the two simulations operate under the same conditions as in the single rotor case with the lower thrust level (Table 1). The vehicle stands with the landing skids touching the ground. The corresponding height of the front rotors above ground is $H/R = 1.31$. Without vertical offset, the rear rotors are located at the same height; with the vertical offset, their height is $H/R = 1.66$. As in the single rotor cases, only the rotors are included in the simulations. The fuselage is not accounted for. The simulations are run in a domain of size $8D \times 8D \times 2.5D$ with a uniform resolution of 48 grid points per rotor radius. 150 rotor revolutions are computed, and the averaging is performed over the last 50 revolutions.

The aim of this example is to locate dangerous areas in the outwash of a quadrotor. For this purpose, we rely on the work by Preston et al. (Ref. 2, Appendix C) who summarized various contributions on the hazardousness of outwash flow for military and civilian personnel. We limit the present discussion to the risk associated with personnel overturning forces and moments. The risk of biophysical injury is not assessed in this example. For military applications, Preston et al. describe the PAXman model that enables a quantitative evaluation of the overturning hazard. For civilian applications, however, no such elaborated metric is reported. Nevertheless, after reviewing multiple works in the literature, they suggest that regions where the average flow velocity exceeds 15 m/s should be approached with caution and regions where it ex-

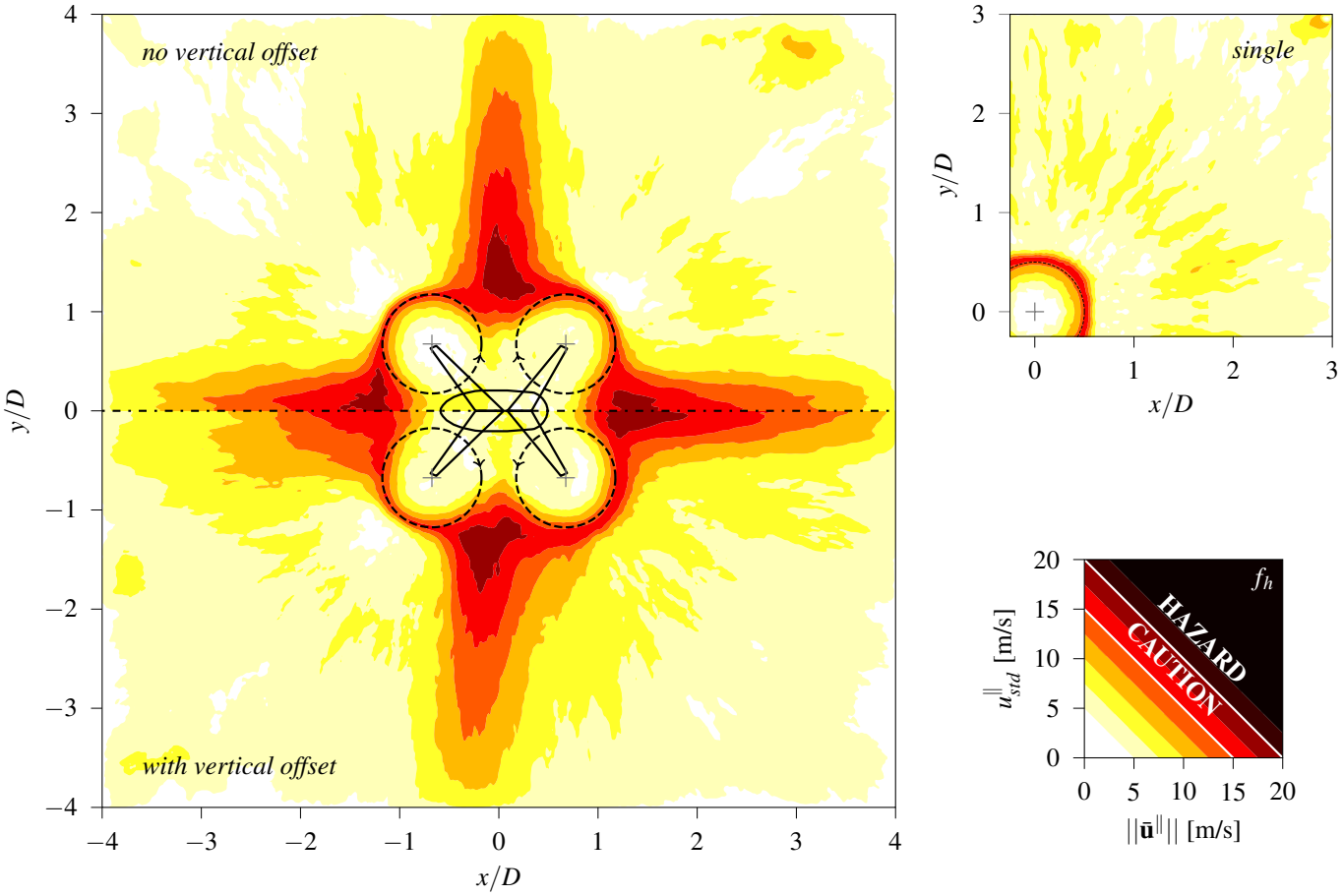

Figure 17: Caution and hazard zones in the vicinity of the quadrotor air taxi hovering on the ground, with and without rotor vertical offset (left); and in the vicinity of the single rotor (top right). The hazardousness factor (bottom right) is based on the average and standard deviation of the velocity parallel to the ground, calculated in a plane three feet above the ground (at $z/R = 0.33$).

ceeds 20 m/s should be considered hazardous. They also note that the existence of flow unsteadiness lowers these limits on the average flow velocity, although no quantitative metric is described.

We propose the definition of a hazardousness factor f_h to merge the criteria based on average flow and unsteadiness. The definition is arbitrary but goes back to the criteria proposed in Ref. 2 in the case of steady flow:

$$f_h = ||\bar{\mathbf{u}}^{\parallel}|| + \beta u_{\text{std}}^{\parallel}, \tag{9}$$

where $\bar{\mathbf{u}}^{\parallel} = \bar{\mathbf{u}} - \bar{u}_z \hat{\mathbf{e}}_z$ is the average velocity vector projected in a plane parallel to the ground, and β is a tunable parameter. For the present illustration, we arbitrarily select $\beta = 1$.

A caution and hazard map is shown in Fig. 17, as a result of the quadrotor air taxi simulations. It is based on the definition of f_h which uses the velocity (average and standard deviation) computed in a plane parallel to the ground and located at a height of three feet. The choice of this height is somewhat arbitrary but stems from the location of the center of pressure of the PAXman model. We argue that the velocity at the center of pressure of a standing human body is representative of the force applied to the body immersed in the outwash flow. A more rigorous evaluation should use PAXman for each (x,y) location on the map. However, model parameters for civilians are currently not available.

Cautionary regions exist in the front, back, left, and right of the vehicle, that is, at the azimuthal angles between the rotors. After inspection of the results, the average outwash velocity in these regions remains significant from the ground up to a height of one radius and above. Importantly, such cautionary regions are not present in the case of a single rotor hovering at $H/R = 1.31$, as shown also in Fig. 17 (top right). They are the product of the aerodynamic interaction between the rotors. In the areas in between the cautionary regions, the rotorwash flow is more similar to the case of the single rotor, with a marked wall jet below $z/R = 0.33$ (not shown in the figure).

Comparing the hazardousness of the two quadrotor designs, the cautionary region in front of the vehicle ($x < 0$) is wider for the vehicle with rotor vertical offset, but the velocities are smaller, reducing f_h. The region with high f_h on the sides is slightly tilted forward in the presence of the vertical offset, but the level of f_h remains similar. This suggests that the offset affects the flow patterns in between the rotors with

different heights, resulting in an outwash velocity that is not purely radial. The region in the back of the vehicle remains similar for the two designs.

Finally, Fig. 17 suggests that approaching the vehicle at a 45° angle from the front left or the front right would provide the least hazardous path for both designs. These preliminary results should, however, be consolidated with the study of more conditions (including the effect of the fuselage), a more rigorous definition of the hazard criterion —today, still a current research topic (Ref. 48)—, and complementary validation against experimental results.

CONCLUSIONS

This work considered the use of CFD for the analysis of rotorwash, the target application being the operation of UAM vehicle IGE. A single rotor was simulated with the high-fidelity solver OVERFLOW and the medium-fidelity VPM method, and the simulations were compared to highlight the effect of various numerical parameters. Additionally, the reference high-fidelity simulation was used to verify the consistency of the modeling approach in the medium-fidelity solver. Owing to their smaller computational intensity, medium-fidelity simulations could then be used to analyze the flow generated by the rotors of a quadcopter air taxi and to highlight the effect of rotor placement (i.e., a design parameter) on the potential hazard caused by the outwash flow. This illustrated how the combined use of such simulations can benefit the development of safe UAM operations.

The conclusions of this study are summarized as follows:

- High-fidelity DDES simulations can be used for the analysis of the flow past a rotor IGE, although at a cost that makes it impractical for trade or parametric studies. We explored the possibility of reducing the order of the numerical schemes and increasing the time step in order to accelerate the simulation without degrading the outwash prediction too much, compared to the recommended high-fidelity settings. From the results we analyzed, it appeared that the use of Δt equal to 1° per time step, and third-order accurate schemes in the wake region are sufficient to capture all the relevant features of the time-averaged flow, as long as a resolution of $h = 0.1\,c_{\text{tip}}$ is used in the entire region of interest. However, other studies showed that a correct prediction of the rotor figure of merit requires a finer time step. Likewise, our results suggested that correctly capturing the velocity fluctuations in the outwash regions requires fine time steps and high-order schemes.

- Medium-fidelity simulations can be used to obtain valuable insights in the outwash flow at a more reasonable cost, hence enabling parametric studies. In particular, we showed that the wall treatment introduced in this work for the VPM method constitutes a satisfactory model to account for the presence of the ground, even when the spatial resolution is too coarse to properly capture the wall boundary layer. However, special attention must be paid to the accuracy of the calculated blade loading, which can deteriorate due to the difficulty of predicting the tip loads. The spatial resolution of 48 particles per rotor radius provided the best trade-off between accuracy and computation cost.

- The necessity of a long averaging time to obtain converged flow statistics in the wall region was emphasized. Ideally, we recommend running simulations for 75 to 100 rotor revolutions, and processing the results by averaging over the last 25 to 50 revolutions (also exploiting flow symmetry, if possible). This should be sufficient to obtain converged statistics on the velocity (average and fluctuations) in a region up to two rotor diameters away from a single rotor. An averaging time corresponding to 10 rotor revolutions is the lower limit. However, these parameters may need to be adapted depending on the wake-generating vehicle, its height, and disk loading.

- The high cost of high-fidelity simulations can be partially mitigated by appropriate start-up procedures. More work is needed to adapt the current guidelines to IGE cases.

- Despite the differences in rotor geometries and operating conditions, our numerical results agreed qualitatively well with experimental data on single rotors available in the literature.

- Extended cautionary regions were discovered in the vicinity of the quadrotor air taxi, due to a fuller outwash velocity profile emanating from between the rotors. Increasing the height of the rear rotors contributed to a slightly lower hazardousness factor that was defined for this work. Regardless of the rotor placement, approaching the vehicle from the front left or right seemed the least hazardous. Nevertheless, we highlighted that more research is needed to determine quantitative metrics to assess the danger of outwash flow for civilians.

Although the simulations presented in this work considered a simple flat ground and rotors only, CFD methods are able of computing the flow past complex geometries —a necessary capability to assess the safety of UAM operation in proximity to vertiports. In this regard, the predictiveness of carefully conducted high-fidelity simulations is now widely recognized. Additionally, we showed that there is an opportunity for less computationally expensive methods to be used for similar engineering applications. However, comparisons against reference simulations and experimental results are needed to verify and validate the various models involved.

ACKNOWLEDGMENTS

D.-G. Caprace is supported by an appointment to the NASA Postdoctoral Program at NASA Ames Research Center, administered by Oak Ridge Associated Universities under contract with NASA. Resources supporting this work were provided by the NASA High-End Computing (HEC) Program through the NASA Advanced Supercomputing (NAS) Division at Ames Research Center. The authors express their deep

gratitude to Profs. Philippe Chatelain and Grégoire Winckelmans (UCLouvain, Belgium) for providing access to the source code of VPM4x.

REFERENCES

1. Johnson, W., and Silva, C., "NASA concept vehicles and the engineering of advanced air mobility aircraft," *The Aeronautical Journal*, 2021, pp. 1–33. DOI: 10.1017/aer.2021.92
2. Preston, J. R., Troutman, S., Keen, E., Silva, M., Whitman, N., Calvert, M., Cardamone, M., Moulton, M., and Ferguson, S. W., "Rotorwash operational footprint modeling," Technical Report RDMR-AF-14-02, US Army RDECOM, 2014.
3. Silva, M., abd Leighton Myers, E. H., Tritschler, J., and Holder, J., "Full-Scale Investigation of Rotor/Obstacle Interactions using an Elevated Fixed Platform," Paper 78-2022-1153, Proceedings of the Vertical Flight Society 78th annual forum, Fort Worth, TX, May 10–12, 2022.
4. Lee, T. E., Leishman, J. G., and Ramasamy, M., "Fluid Dynamics of Interacting Blade Tip Vortices with a Ground Plane," *Journal of the American Helicopter Society*, Vol. 55, (2), 2010, pp. 22005. DOI: doi:10.4050/JAHS.55.022005
5. Tanner, P. E., Overmeyer, A. D., Jenkins, L. N., Yao, C.-S., and Bartram, S. M., "Experimental investigation of rotorcraft outwash in ground effect," Paper NF1676L-21054, Proceedings of the AHS International Annual Forum & Technology Display, Virginia Beach, VA, May 5–7, 2015.
6. Ramasamy, M., and Yamauchi, G. K., "Using Model-Scale Tandem-Rotor Measurements in Ground Effect to Understand Full-Scale CH-47D Outwash," *Journal of the American Helicopter Society*, Vol. 62, (1), 2017, pp. 1–14. DOI: doi:10.4050/JAHS.62.012004
7. Dekker, H. N. J., Ragni, D., Baars, W. J., Scarano, F., and Tuinstra, M., "Aerodynamic Interactions of Side-by-Side Rotors in Ground Proximity," *AIAA Journal*, Vol. 60, (7), 2022, pp. 4267–4277. DOI: 10.2514/1.J061105
8. Narducci, R. P., and Hariharan, N. S., "A Common Simulation for Hover Validation of a Helicopter near the Ground," Proceedings of the AIAA SCITECH Forum, National Harbor, MD & online, January 23–27, 2023. DOI: 10.2514/6.2023-1187
9. Ramasamy, M., Potsdam, M., and Yamauchi, G. K., "Measurements to understand the flow mechanisms contributing to tandem-rotor outwash," Paper ARC-E-DAA-TN21861, Proceedings of the AHS 71st annual forum, Virginia Beach, VA, May 21–23, 2015.
10. Chirico, G., Szubert, D., Vigevano, L., and Barakos, G. N., "Numerical modelling of the aerodynamic interference between helicopter and ground obstacles," *CEAS Aeronautical Journal*, Vol. 8, (4), 2017, pp. 589–611. DOI: 10.1007/s13272-017-0259-y
11. Merabet, R., and Laurendeau, E., "Numerical simulations of a rotor in confined areas including the presence of wind," *Aerospace Science and Technology*, Vol. 126, 2022, pp. 107657. DOI: https://doi.org/10.1016/j.ast.2022.107657
12. Zhao, J., and He, C., "Physics-Based Modeling of Viscous Ground Effect for Rotorcraft Applications," *Journal of the American Helicopter Society*, Vol. 60, (3), 2015, pp. 1–13. DOI: doi:10.4050/JAHS.60.032006
13. Tan, J. F., Sun, Y. M., and Barakos, G. N., "Vortex Approach for Downwash and Outwash of Tandem Rotors in Ground Effect," *Journal of Aircraft*, Vol. 55, (6), 2018, pp. 2491–2509. DOI: 10.2514/1.C034740
14. Andronikos, T., Papadakis, G., Riziotis, V. A., Prospathopoulos, J. M., and Voutsinas, S. G., "Validation of a cost effective method for the rotor-obstacle interaction," *Aerospace Science and Technology*, Vol. 113, 2021, pp. 106698. DOI: https://doi.org/10.1016/j.ast.2021.106698
15. Moushegian, A. M., and Smith, M. J., "Physics and Accuracy of Dual-Solver Simulations of Rotors in Ground Effect," *Journal of the American Helicopter Society*, Vol. 68, (1), 2023, pp. 1–16. DOI: doi:10.4050/JAHS.68.012010
16. Ventura Diaz, P., Johnson, W., Ahmad, J., and Yoon, S., "The Side-by-Side Urban Air Taxi Concept," Paper AIAA 2019-2828, Proceedings of the AIAA Aviation Forum, Dallax, TX, June 17–21, 2019. DOI: 10.2514/6.2019-2828
17. Ventura Diaz, P., and Yoon, S., "High-Fidelity Simulations of a Quadrotor Vehicle for Urban Air Mobility," Paper AIAA 2022-0152, Proceedings of the AIAA SCITECH Forum, San Diego, CA, January 3–7, 2022. DOI: 10.2514/6.2022-0152
18. Garcia Perez, D., Ventura Diaz, P., and Yoon, S., "A Comparison of Rotor Disk Modeling and Blade-Resolved CFD Simulations for NASA's Tiltwing Air Taxi," Proceedings of the 79th VFS annual forum, West Palm Beach, FL, May 16–18, 2023.
19. Chaderjian, N. M., and Ahmad, J., "Navier-Stokes Assessment of Test Facility Effects on Hover Performance," Proceedings of the 71st Annual Forum of the American Helicopter Society, Virginia Beach, VA, May 5–7 2015.
20. Chaderjian, N. M., "Quantitative Approach for the Accurate CFD Simulation of Hover in Turbulent Flow," Paper ICCFD11-0603, International Conference on Computational Fluid Dynamics 11, July 2022.
21. Caprace, D.-G., Chatelain, P., and Winckelmans, G., "Wakes of rotorcraft in advancing flight: A large eddy simulation study," *Physics of Fluids*, Vol. 32, (8), 2020, pp. 087107. DOI: 10.1063/5.0015162
22. Caprace, D.-G., Winckelmans, G., and Chatelain, P., "Assessment of the Vortex Particle-Mesh Method for Efficient LES of Hovering Rotors and their Wakes," Paper AIAA 2021-0738, Proceedings of the AIAA Scitech Forum, Online Event, January 11–15 & 19–21, 2021. DOI: 10.2514/6.2021-0738
23. Caprace, D.-G., and Ning, A., "Large Eddy Simulation of the Wakes of Three Urban Air Mobility Vehicles," Paper 78-2022-0063, Proceedings of the Vertical Flight Society 78th annual forum, Fort Worth, TX, May 10–12, 2022.
24. Caprace, D.-G., Ning, A., Chatelain, P., and Winckelmans, G., "Effects of rotor-airframe interaction on the aeromechanics and wake of a quadcopter in forward flight," *Aerospace Science and Technology*, 2022, pp. 107899. DOI: https://doi.org/10.1016/j.ast.2022.107899
25. Pulliam, T., "High Order Accurate Finite-Difference Methods: as seen in OVERFLOW," Paper AIAA 2011-3851, Proceedings of the 20th AIAA Computational Fluid Dynamics Conference, Honolulu, HI, June 27–30, 2011. DOI: 10.2514/6.2011-3851
26. Jespersen, D., Pulliam, T., Buning, P., Jespersen, D., Pulliam, T., and Buning, P., "Recent enhancements to OVERFLOW," Proceedings of the 35th Aerospace Sciences Meeting and Exhibit, Reno, NV, January 6–9, 1997. DOI: 10.2514/6.1997-644
27. Ventura Diaz, P., and Yoon, S., "Computational Study of NASA's Quadrotor Urban Air Taxi Concept," Paper AIAA 2020-0302, Proceedings of the AIAA Scitech Forum, Orlando, FL, January 2020. DOI: 10.2514/6.2020-0302
28. Chan, W., Gomez, R., Rogers, S., and Buning, P., "Best Practices in Overset Grid Generation," Paper AIAA 2002-3191, Proceedings of the 32nd AIAA Fluid Dynamics Conference, St. Louis, MO, June 24–26, 2002. DOI: 10.2514/6.2002-3191
29. Chatelain, P., and Koumoutsakos, P., "A Fourier-based elliptic solver for vortical flows with periodic and unbounded directions," *Journal of Computational Physics*, Vol. 229, (7), 4 2010, pp. 2425–2431. DOI: 10.1016/j.jcp.2009.12.035
30. Caprace, D.-G., Gillis, T., and Chatelain, P., "FLUPS: A Fourier-Based Library of Unbounded Poisson Solvers," *SIAM Journal on Scientific Computing*, Vol. 43, (1), January 2021, pp. C31–C60. DOI: 10.1137/19M1303848
31. Jeanmart, H., and Winckelmans, G., "Investigation of eddy-viscosity models modified using discrete filters: A simplified regularized variational multiscale model and an enhanced field model," *Physics of Fluids*, Vol. 19, (5), May 2007, pp. 055110. DOI: 10.1063/1.2728935
32. Cocle, R., Bricteux, L., and Winckelmans, G., "Scale dependence and asymptotic very high Reynolds number spectral behavior of multiscale subgrid models," *Physics of Fluids*, Vol. 21, (8), Aug 2009, pp. 085101. DOI: 10.1063/1.3194302

33. Cocle, R., Dufresne, L., and Winckelmans, G., "Investigation of multiscale subgrid models for LES of instabilities and turbulence in wake vortex systems," *Lecture Notes in Computational Science and Engineering*, Vol. 56, 2007, pp. 141–159.

34. Winckelmans, G. S., *Encyclopedia of Computational Mechanics*, John Wiley & Sons, Ltd, 2004, Chapter Vortex Methods, pp. 129–153. DOI: 10.1002/0470091355.ecm055

35. Chatelain, P., Curioni, A., Bergdorf, M., Rossinelli, D., Andreoni, W., and Koumoutsakos, P., "Billion vortex particle Direct Numerical Simulations of aircraft wakes," *Computer Methods in Applied Mechanics and Engineering*, Vol. 197, (13), Feb 2008, pp. 1296–1304. DOI: 10.1016/j.cma.2007.11.016

36. Mimeau, C., and Mortazavi, I., "A Review of Vortex Methods and Their Applications: From Creation to Recent Advances," *Fluids*, Vol. 6, (2), 2021. DOI: 10.3390/fluids6020068

37. Cottet, G.-H., and Koumoutsakos, P., *Vortex Methods, Theory and Practice*, Cambridge University Press, 2000.

38. Sbalzarini, I. F., Walther, J. H., Bergdorf, M., Hieber, S. E., Kotsalis, E. M., and Koumoutsakos, P., "PPM A highly efficient parallel particle mesh library for the simulation of continuum systems," *J. Comput. Phys.*, Vol. 215, jul 2006, pp. 566–588. DOI: 10.1016/j.jcp.2005.11.017

39. Caprace, D.-G., Winckelmans, G., and Chatelain, P., "An immersed lifting and dragging line model for the vortex particle-mesh method," *Theoretical and Computational Fluid Dynamics*, Vol. 34, 2020, pp. 21–48. DOI: 10.1007/s00162-019-00510-1

40. Lepot, C., *Implementation and validation of symmetry and no-slip boundary conditions in a 3-D vortex particle-mesh method*, Master's thesis, Université catholique de Louvain, 2019.

41. van Rees, W. M., Leonard, A., Pullin, D. I., and Koumoutsakos, P., "A comparison of vortex and pseudo-spectral methods for the simulation of periodic vortical flows at high Reynolds numbers," *Journal of Computational Physics*, Vol. 230, (8), 2011, pp. 2794–2805. DOI: 10.1016/j.jcp.2010.11.031

42. Chatelain, P., Backaert, S., Winckelmans, G., and Kern, S., "Large eddy simulation of wind turbine wakes," *Flow, Turbulence and Combustion*, Vol. 91, (3), 2013, pp. 587–605. DOI: 10.1007/s10494-013-9474-8

43. Lee, M., and Moser, R. D., "Direct numerical simulation of turbulent channel flow up to $Re_\tau \approx 5200$," *Journal of Fluid Mechanics*, Vol. 774, 2015, pp. 395–415. DOI: 10.1017/jfm.2015.268

44. Yoon, S., Chaderjian, N. M., Pulliam, T. H., and Holst, T. L., "Effect of Turbulence Modeling on Hovering Rotor Flows," Paper AIAA 2015-2766, Proceedings of the 45th AIAA Fluid Dynamics Conference, Dallas, TX, June 22–26, 2015. DOI: 10.2514/6.2015-2766

45. Yoon, S., Lee, H. C., and Pulliam, T. H., "Computational Analysis of Multi-Rotor Flows," Paper AIAA 2016-0812, Proceedings of the 54th AIAA Aerospace Sciences Meeting, San Diego, CA, January 4–8, 2016. DOI: 10.2514/6.2016-0812

46. Glauert, M. B., "The wall jet," *Journal of Fluid Mechanics*, Vol. 1, (6), 1956, pp. 625–643. DOI: 10.1017/S002211205600041X

47. Silva, M., and Riser, R., "CH-47D tandem rotor outwash survey," Proceedings of the 67th Annual Forum of the American Helicopter Society, Virginia Beach, VA, May 3–5, 2011.

48. Calvert, M. E., and Wenren, Y., "Rotorcraft Outwash and Human Stability," Paper AIAA 2019-1095, Proceedings of the AIAA Scitech Forum, San Diego, CA, January 7–11, 2019. DOI: 10.2514/6.2019-1095